

Article

# Electrochemical Impedance Spectroscopy Accuracy and Repeatability Analysis of 10 kWh Automotive Battery Module

Manuel Kasper <sup>1,\*</sup>, Arnd Leike <sup>2</sup>, Nawfal Al-Zubaidi R-Smith <sup>1</sup>, Aikaterini Papachristou <sup>2</sup> and Ferry Kienberger <sup>1</sup>

<sup>1</sup> Keysight Laboratories, Keysight Technologies Austria GmbH, 4020 Linz, Austria; ferry\_kienberger@keysight.com (F.K.)

<sup>2</sup> BMW Group, BMW AG München, 80788 München, Germany; aikaterini.papachristou@bmw.de (A.P.)

\* Correspondence: manuel.kasper@keysight.com

## Abstract

Electrochemical Impedance Spectroscopy (EIS) measurements are highly sensitive to the fixturing, temperature, and state of charge (SoC) of batteries. For 10 kWh automotive battery modules, we show that variations in SoC and temperature introduce significant errors at low-to-medium frequencies (<100 Hz), while improper fixture wiring affects mainly higher-frequency accuracy, with errors up to 100% in the imaginary part at 1 kHz. In addition, we study repeatability across various tester-module configurations. EIS results remain highly consistent ( $\pm 100 \mu\Omega$ ) across three different modules. Comparing the same module across two different testers, deviations are even lower ( $\pm 30 \mu\Omega$  up to 1 kHz). The EIS evolution is studied with respect to the cycle numbers, where a strong correlation of low-frequency impedance features is demonstrated. A new combined quotient feature is introduced and suggested as a reliable and efficient state of health (SoH) indicator, solely based on a model-free and phenomenological approach. The study demonstrates the potential of EIS as a powerful tool for battery module characterization, provided that its requirements and limitations are carefully addressed through well-defined experimental setups. Accurate and repeatable EIS measurements are particularly important for obtaining accurate electrochemical insights, especially in the low-to-mid frequency domain, where impedance variations are most sensitive to battery states and ageing effects.



Academic Editor: Xianglin Li

Received: 2 September 2025

Revised: 1 October 2025

Accepted: 11 October 2025

Published: 23 October 2025

**Citation:** Kasper, M.; Leike, A.; Al-Zubaidi R-Smith, N.; Papachristou, A.; Kienberger, F. Electrochemical Impedance Spectroscopy Accuracy and Repeatability Analysis of 10 kWh Automotive Battery Module. *Batteries* **2025**, *11*, 389. <https://doi.org/10.3390/batteries1110389>

**Copyright:** © 2025 by the authors. Licensee MDPI, Basel, Switzerland. This article is an open access article distributed under the terms and conditions of the Creative Commons Attribution (CC BY) license (<https://creativecommons.org/licenses/by/4.0/>).

**Keywords:** electrochemical impedance spectroscopy (EIS); lithium-ion battery module; measurement uncertainty; state of health (SoH)

## 1. Introduction

Lithium-ion batteries (LiBs) power modern electric vehicles (EVs), and the electrical, mechanical, and thermal characterization of the individual cells, modules, and packs is of high relevance [1,2]. While a considerable amount of research has focused on cell-level performance testing [3], module-level performance testing is less explored, especially regarding accuracy and repeatability for quality inspection and second-life applications [4]. Reliable characterization of battery modules under real-world conditions is essential for both first-life and second-life applications [5]. Therefore, advanced diagnostic techniques are necessary to efficiently assess module performance, cycling ageing, and degradation mechanisms [6]. One of the promising methods is electrochemical impedance spectroscopy (EIS), which provides key insights into the battery state, also allowing accurate performance assessments [7]. In battery research, EIS enables detailed characterization of electrochemical

processes, including the study of fundamental reaction mechanisms. For single cells, EIS is extensively applied to assess the condition of active materials, monitor degradation [8], and evaluate the state of health (SoH) [9].

Accurate EIS is critical for characterizing battery cells and modules, especially as cell impedances reach the micro-ohm ( $\mu\Omega$ ) range [10]. Given the wide frequency range of EIS from milli Hertz to tens of kilo Hertz, identifying and mitigating measurement errors across the full frequency range is essential [7]. EIS errors stem from both systematic and random sources. Systematic errors, such as calibration deviations and environmental interference, can be corrected, whereas random errors, arising from electronic drift, fixture variations, or electromagnetic noise, are more challenging to control. Additionally, the temperature dependence of the electrical impedance requires precise environmental control. Consequently, obtaining precise and reliable EIS data is essential for assessing battery performance against international standards and metrological requirements, such as the GTR No. 22 regulatory framework, which defines minimum durability requirements for in-vehicle batteries [11,12]. Furthermore, as the EU's Battery Passport initiative aims to enhance battery lifecycle transparency and sustainability, standardized and traceable impedance measurements will play a key role in ensuring compliance with performance, safety, and durability [13].

This study aims to investigate the accuracy and repeatability of EIS measurements for EV battery modules by addressing key challenges related to fixture configurations, temperature stability, and state-of-charge (SoC) control. By testing three 10 kWh modules, we provide a systematic EIS error analysis, including the impact of wiring, temperature, and SoC, as well as various tester configurations. These findings confirm EIS as a reliable tool for battery module characterization, provided that precision metrology principles ensure measurement accuracy and repeatability.

## 2. Materials and Methods

### 2.1. Module Test Hardware

The test setup (Figure 1) consists of a two-channel Keysight, Santa Rosa, CA, USA SL1001A module tester and a temperature-controlled safety environment, including a fluid conditioning unit for enhanced thermal management. Each channel is configured to handle a maximum voltage of 200 V and maximum current of 750 A. For precise EIS measurements, a four-wire Kelvin connection is used between the module tester and the battery module through a connection box. The force connections utilize cables with a cross-section of  $100 \text{ mm}^2$ , minimizing Joule heating losses. The separate sense connections maintain accurate voltage measurements across the module by compensating for resistive losses in the force cables. The module has an 8S5P configuration (300 Ah unit with a nominal voltage of 33.5 V and a total capacity of 10 kWh) and is equipped with a water-cooled heat exchanger to support additional thermal regulation. Temperature stabilization within the chamber is maintained through a controlled air flow system operating at a constant temperature. Multiple temperature sensors (K-type thermocouples) are placed across the module to continuously monitor and log temperature data for safety supervision. Voltage monitoring is conducted for the complete module and for each of the 8 serially connected cell blocks via dedicated channels. The system is equipped with an automated safety supervision mechanism that monitors critical parameters, including individual cell voltages, current levels, and cell temperatures. In the event of any imbalance or abnormal readings, the tester is automatically shut down and remains in a safe state with the battery module disconnected. This approach ensures protection against potential thermal runaway and electrical faults, thereby maintaining a safe and controlled testing environment. In this study, two identical testers, tester 1 and tester 2, were utilized.

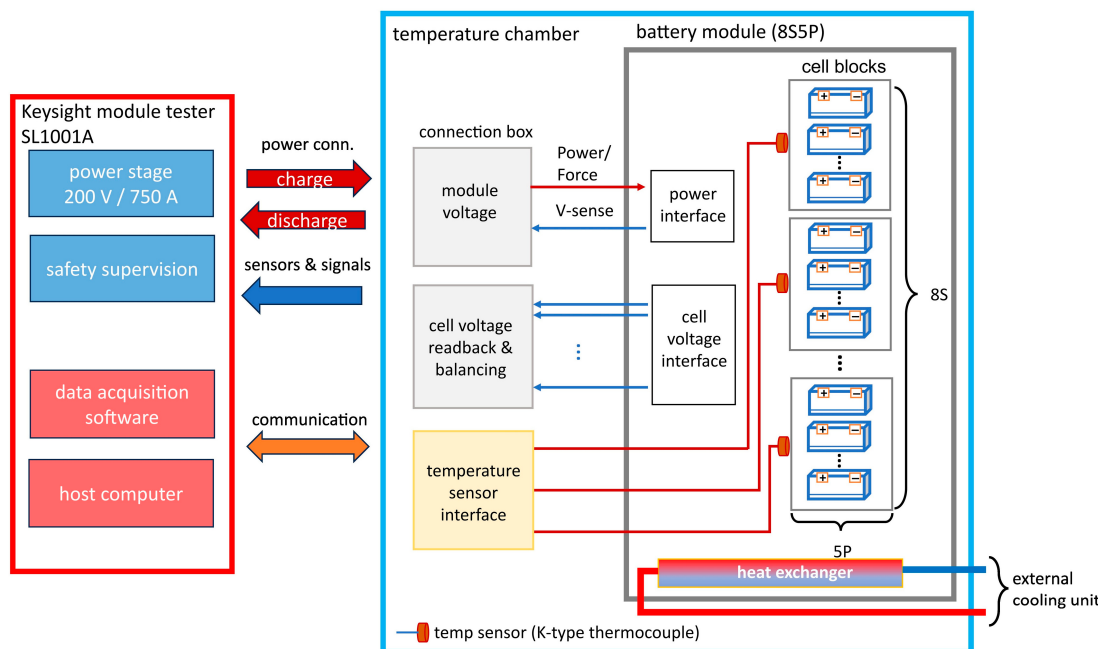


**Figure 1.** Schematic of the test setup consisting of a two-channel Keysight SL1001A module tester integrated in a temperature-controlled safety environment with a fluid conditioning unit. Voltage measurements for each cell block are independently acquired through separate measurement channels. In case of imbalances or abnormal readings, the system is automatically shut down and remains in a safe state.

## 2.2. Electrical Fixture and EIS Calibration

For accurate and repeatable EIS measurements, both a calibrated test system and an optimized wiring scheme to minimize random error contributions are established (Figure 2). The test setup employs a four-wire Kelvin configuration using separate force and sense cables. Electrical connections to the battery module are established via screw terminals, with specialized lugs for the force wiring. Figure 2a shows a sketch of the contact terminals at the module interface. Due to the high test-current requirements, two parallel conductors are utilized for both the positive and negative connections. The force cables are terminated at a connection box mounted on the inner rear side of the thermal chamber. While twisting the force cables is not possible, the positive and negative conductors are positioned as closely as possible to reduce mutual magnetic coupling. Figure 2c shows a picture of the electrical fixture to the battery module. The sense connections, used to detect the voltage drop across the battery module without carrying significant current, are prepared using thin and flexible cables configured in twisted pairs to mitigate magnetic coupling in the relevant frequency range.

EIS measurements are performed by applying an alternating current (AC) signal in galvanostatic mode to the battery module and recording the system response, specifically the voltage drop  $v(t)$  across the battery terminals and the current  $i(t)$  through the battery. A sinusoidal current source, in conjunction with a power amplifier, generates the required excitation current amplitude to stimulate the battery. The sense cables are used for the acquisition of the response voltage  $v(t)$ . During signal acquisition, the DC component of the measured voltage is removed, and the remaining AC component is amplified. Both the current  $i(t)$  and voltage  $v(t)$  signals are digitized using a two-channel analog-to-digital converter (ADC) operating at a maximum sampling rate of 1 MHz, ensuring that each sinusoidal signal is sampled at least 10 times per cycle. Calibration of the EIS system is achieved by connecting known impedance standards to the force and sense cables while maintaining the reference geometry, as shown in Figure 2c. An adapter with

BNC connections facilitates the calibration. The calibration spans a frequency range from 50 mHz to 5 kHz and incorporates three standards, including a short circuit (defined as  $Z_{d\text{Short}} = 0 \Omega$ ) and two coaxial shunt standards with a known resistance value (10 mΩ and 100 mΩ nominal values). Raw impedance measurements ( $Z_{mR1}$ ,  $Z_{mR2}$ , and  $Z_{m\text{Short}}$ ) are obtained for these standards and compared with their defined impedance values ( $Z_{dR1}$ ,  $Z_{dR2}$ , and  $Z_{d\text{Short}}$ ) to compute three error coefficients (see Figure 2b). These coefficients are then applied to correct the raw impedance measurements of the DUT ( $Z_{m\text{DUT}}$ ), yielding the calibrated impedance ( $Z_{c\text{DUT}}$ ) [7,14]. Figure 2d shows the extent of correction in a Nyquist plot at a medium SoC in a limited frequency range of 50 mHz to approximately 2 kHz. The raw data (red trace) shows significant differences compared to the corrected data (blue trace), particularly at frequencies above 100 Hz. An inset plot displays the vector difference magnitude on a logarithmic scale from 10 Hz to 5 kHz. The difference between raw data and corrected data exceeds the noise level of  $\sim 50 \mu\Omega$  at 100 Hz and further increases to  $\sim 800 \mu\Omega$  at 1 kHz, which corresponds to 30% of the module's absolute impedance of 2.5 mΩ. At 5 kHz, the amount of correction reaches about 50 mΩ.

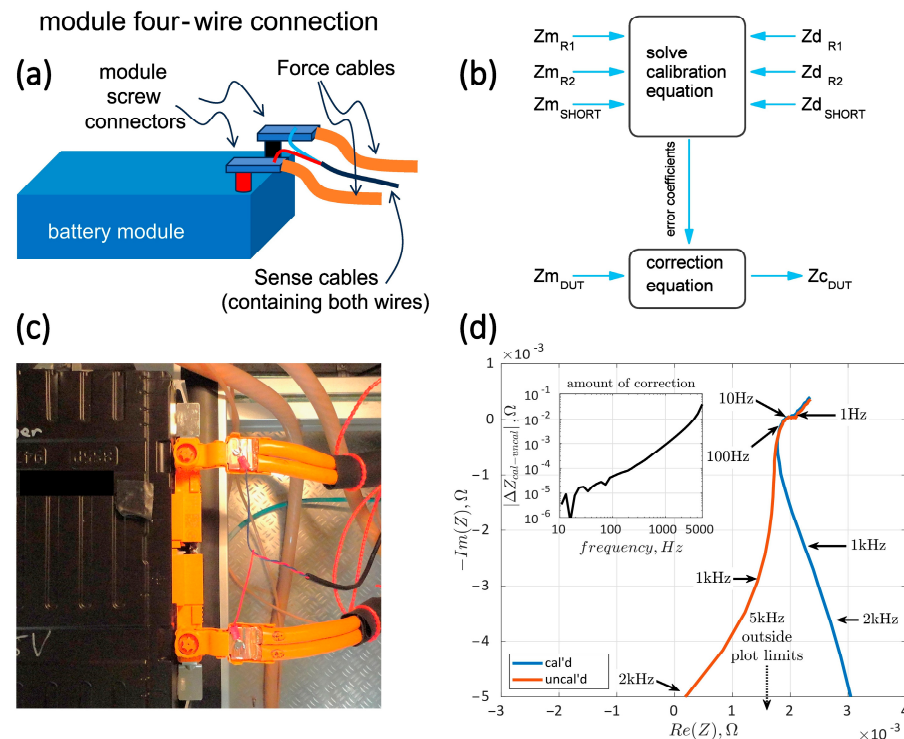


**Figure 2.** EIS wiring scheme and calibration designed to minimize random error contributions. **(a)** Sketch of the connection setup for the force and sense cables. Electrical contact to the battery module is established using screw terminals. **(b)** The impedance calibration and correction concept. Known impedance standards are connected to the force and sense cables while preserving the reference geometry. **(c)** Picture of the electrical fixture. **(d)** Nyquist plot showing the comparison of the raw and calibrated module impedance in the frequency range of 50 mHz to approximately 2 kHz. The plot range was limited for the sake of clarity. The inset highlights the magnitude of the vector difference on a logarithmic scale from 10 Hz to 5 kHz.

Temperature readings are synchronized with the test plan through coherent data acquisition by the module tester. Multiple temperature sensors are distributed across the battery module to monitor and capture the temperature spread, ensuring accurate thermal tracking during impedance measurements.

### 2.3. Battery Modules and Cells

The experiments utilize three battery modules, labelled as Module 1, Module 2, and Module 3. The modules consist of prismatic Li-ion cells with a nominal capacity of 60 Ah composed of a graphite anode and a Lithium–Nickel–Cobalt–Manganese–Oxide ( $\text{LiNiCoMnO}_2$ ) cathode. The topology of the modules is 8S5P. This results in 300 Ah with a nominal voltage of 33.5 V and a total energy capacity of 10 kWh. The modules are subjected to 300 charge–discharge cycles prior to testing, and an additional fresh module with only few (<5) prior cycles is used for comparisons. For simplicity, the fresh module is labelled with ‘cycle 0’ subsequently. The experimental tests of the three battery modules are conducted using two identical test setups. Tester 1 is connected to Module 1 and Module 2 (on Channel 1 and Channel 2, respectively), while Tester 2 is connected to Module 3 (on Channel 1).

## 3. Results and Discussion

### 3.1. Module Cycling and EIS Measurement Workflow

The modules were placed in temperature-controlled chambers and installed using a four-wire fixture to maintain precise electrical connections. Impedance calibration was performed at room temperature, including the calculation of error coefficients and the correction of the raw impedance (see Materials and Methods). After EIS calibration, a predefined temperature was set, and the modules were allowed to rest for 24 h to achieve thermal stability (which is a multiple of the thermal time constant obtained from control experiments). An extended test plan was executed (Figure 3). The open-circuit voltage (OCV) curve was determined using a C/20 discharge step, followed by a standard full charge at 1 C. After a one-hour rest period, the first of 11 subsequent EIS measurements was conducted at a state of charge (SoC) of 100%. Sequential 10% discharge steps at a 1 C rate were applied to cover the entire SoC range down to 0%. The discharge capacity was calculated based on the OCV measurement and adapted to account for variations in discharge rates. EIS measurements were acquired at each discharge step, generating parametric impedance spectroscopy data as a function of SoC and cycle number. After the extended test, 50 charge/discharge cycling sequences were performed with 1 C rate (corresponding to 300 A), and the extended measurement routine was repeated. The process was repeated until a total of 500 cycles was reached.

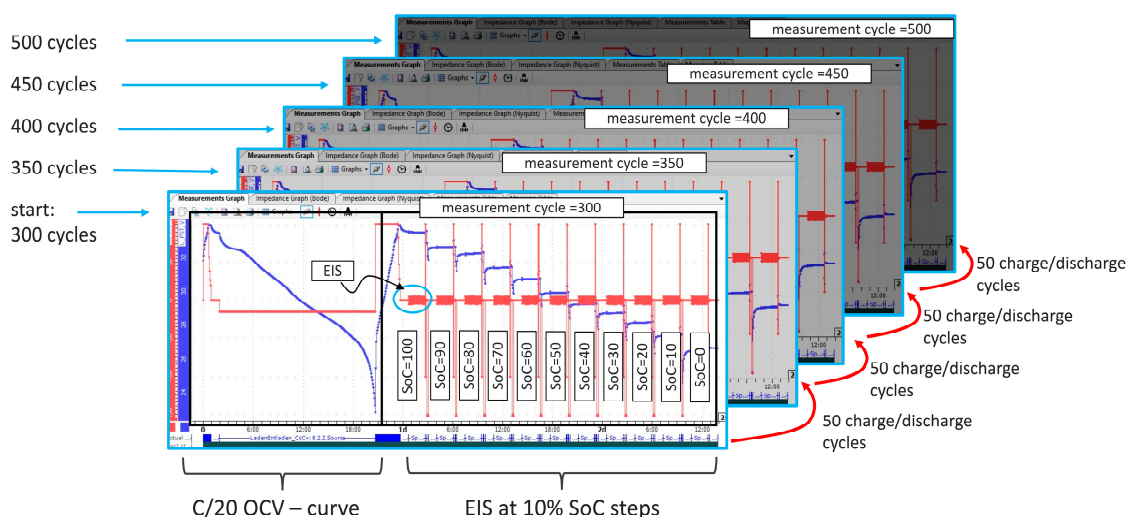


**Figure 3.** Experimental EIS cycling study. At the beginning, the three precycled (300 cycles) modules are characterized by an extended measurement cycle. The cycle starts with a C/20 discharge to determine the OCV curve, followed by a full 1 C charge step. After a 1 h stabilization period, the first out of 11 EIS measurements was performed at 100% SoC. Subsequent 10% discharge steps at 1 C were conducted to cover the entire SoC range. This was repeated every 50 cycles, from cycle #300 to cycle #500.

### 3.2. EIS Error Analysis for Three Different Fixtures

Accurate EIS measurements require precise fixture preparation and stable environmental conditions to ensure reliable and reproducible data. Here, we show an EIS error analysis for three different fixture configurations (Figure 4). The three different fixture wirings are shown in Figure 4a. In the first scenario, the wiring is correctly executed. Force and sense connections are separated, and the sense wires are twisted to minimize mutual coupling effects, ensuring accurate impedance measurements. In the second scenario, a wrong sense point is used, where the sense cables are connected at some distance over the force cables. This setup reduces measurement accuracy by introducing voltage measurement errors due to current-induced drops added by the force cables. In the third scenario, loose sense wires are used, which results in a significant change in the wiring geometry with respect to the situation when the calibration is performed. In the corresponding EIS curves (Figure 4b), the correct wiring (blue traces) serves as the baseline for comparison with the other two fixture configurations. Significant deviations in the real part are observed, particularly at mid to high frequencies, with differences of up to 45% at 5 kHz for the second configuration and 14% for the third configuration. At low frequencies, the real part error stays within 2–5%. The imaginary part is mainly affected at higher frequencies due to the inductive nature of the most significant error mechanism, resulting in a linear increase in the imaginary error over frequency. Notably, already at 1 kHz, the imaginary error reaches approximately 40% for the second configuration and almost 100% for the third configuration.

### 3.3. EIS Error Analysis Including Temperature and SoC

Accurate EIS measurements require not only correct wiring, as shown in the previous chapter, but also careful DUT preparation to ensure reliable impedance data. Deviations in environmental conditions or improper setup of the battery module can introduce significant errors to the EIS, also at low frequencies. Figure 5 shows the impact of DUT conditioning errors, in particular the temperature and the SoC, on EIS measurements of a battery module. Figure 5a presents the real part of the impedance (resistance), while Figure 5b displays the imaginary part (reactance), with the frequency axis split into two panels for improved visualization. A reference measurement taken at 50% SoC and 23 °C is shown by the blue trace, serving as the baseline for comparison. A subsequent measurement at the same SoC but at a reduced temperature of 20 °C (red trace) shows a noticeable increase in the real part of the impedance at low and medium frequencies, on average 6%. In a subsequent measurement, the SoC is reduced from 50% to 30% while keeping the temperature constant at 23 °C (yellow trace). Significant deviations are thereby observed, particularly in the low-frequency region below 1 Hz, including both the real and imaginary components. In general, the high-frequency components remain relatively unaffected by both the temperature and the SoC. This stability is attributed to the dominance of the inductive and some ohmic characteristics at higher frequencies, which are less sensitive to module conditioning variations.

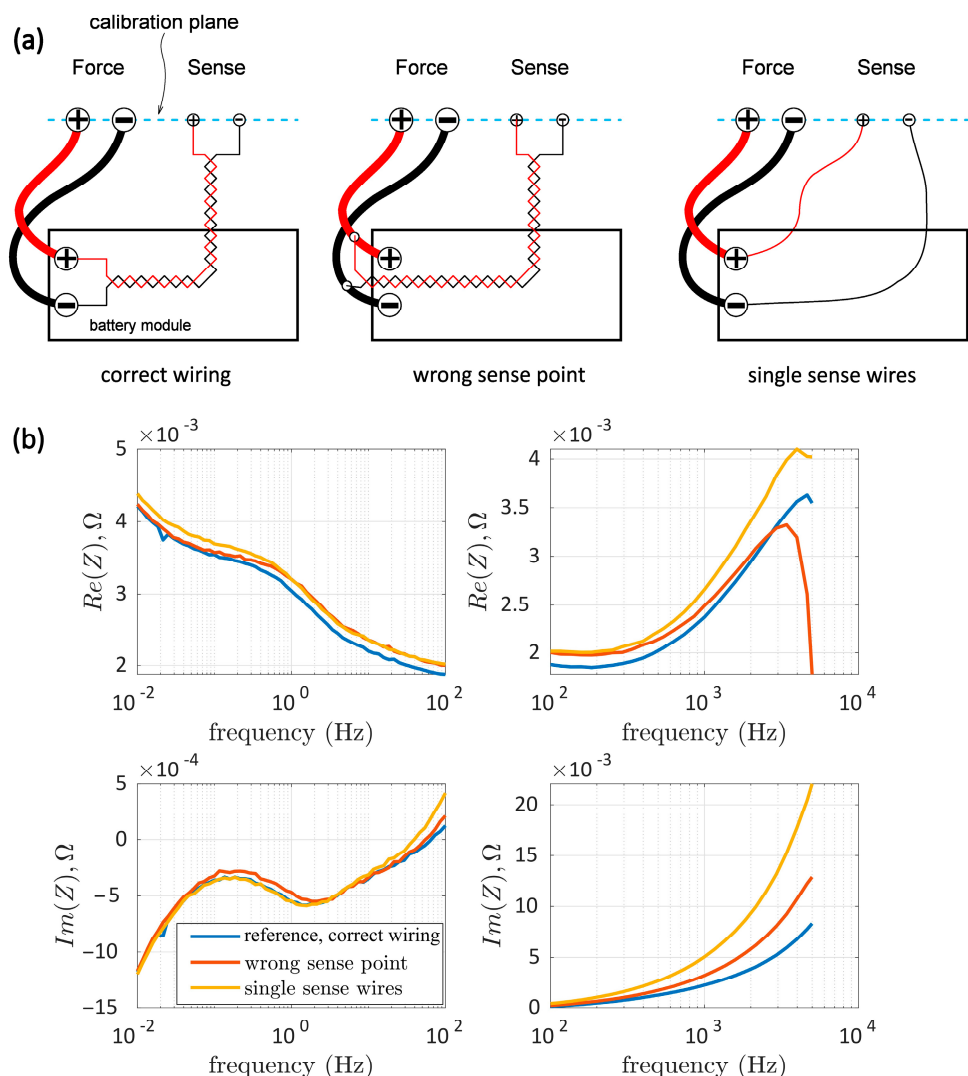


**Figure 4.** (a) Error analysis for three different module fixture wiring configurations. Left: correct wiring with twisted sense wired up to the contact point directly at the battery module. Middle: wrong sense point wiring where the sense pickup is installed over the force cables at some distance to the battery module terminals. Right: single sense untwisted wires for the sense circuit are used. (b) The real and imaginary impedance for the three configurations measured at 50% SoC at constant room temperature. The frequency axis is split between the left and right panels to allow for different axis scaling for low and high frequencies.

### 3.4. EIS Results from Five Different Tester Module Configurations

Calibrated EIS measurements were performed on three battery modules and two testers (Figure 6), resulting in five different configurations, allowing us to assess measurement consistency and test system variations. All modules were cycled to 500 cycles, and measurements were conducted at 50% SoC and 20 °C using best practice wiring schemes.

Figure 6a shows the mapping of the battery modules to the module testers. Battery module 1 measured at channel 1 of tester 1 was arbitrarily defined as the reference configuration (blue). The corresponding impedance is shown in Figure 6b, with the minimum of the real part at approximately 2 mΩ. The second configuration (red) was measured directly after the reference measurement without removing the battery module from the tester. As such, no additional errors from wiring changes or temperature drift affected the measurement.

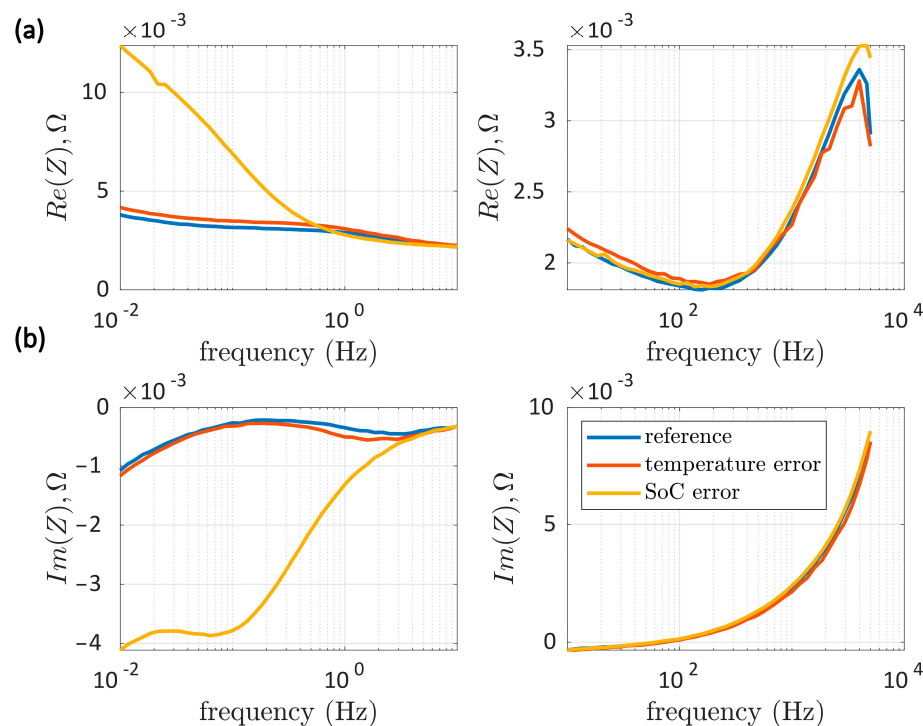


**Figure 5.** Impact of temperature and SoC on EIS measurements. Frequency response of the (a) real and (b) imaginary components of the impedance. The frequency axis is split between the left and right panels to allow for different axis scaling for low and high frequencies. The blue trace represents the reference measurement of Module 1 at 50% SoC and 23 °C. The red trace shows the measurement at 50% SoC and 20 °C. The yellow trace corresponds to a measurement at 30% SoC and 23 °C.

Figure 6c shows the differences in configurations #2–5 against the reference configuration, with the colour of the traces matching with Figure 6a. The frequency axes are divided for low ( $<1$  kHz) and high frequencies ( $>1$  kHz) to allow for optimized y-scaling. Additionally, the accuracy specification of the module tester (Keysight SL1001A, 750 A) is added as dashed line, with an absolute magnitude error of  $\pm 200 \mu\Omega$ , a phase error of  $\pm 2^\circ$ , and a relative error of  $\pm 1\%$  [15]. The relative error term generates the specific shape of the accuracy boundaries, following the measured impedance. Only minimal differences between individual measurements are visible at frequencies up to 2 kHz. From 2 to 5 kHz, deviations are obtained both in the real and the imaginary part of the impedance, caused by small geometrical changes in the cables, the fixture, and the battery during module reinstallation. Measurements involving different modules (Figure 6c; fourth and fifth configurations) show noticeable variations, starting already slightly below 2 kHz. Despite these variations, measurements remain within  $\pm 100 \mu\Omega$  for both the real and imaginary parts within the relevant frequency range of 50 mHz to 1 kHz. Notably, comparisons involving the same module and two different testers stay within  $\pm 30 \mu\Omega$  for frequencies up to 1 kHz.

### 3.5. Evolution of Distinct EIS Features over Cycling Number

Figure 7 presents a Nyquist plot of EIS measurements for a single module at different cycle numbers, starting from 300, 400, 450, and 500, all recorded at 50% SoC. Four distinct impedance features are highlighted and taken from the experimental data without a model fit. The four experimentally determined impedance features are strongly related to the cycle number, including the local minimum of the imaginary impedance, which is related to the width of the semicircle, and the impedance at the specific frequencies of 0.01 Hz, 0.1 Hz, and 3 Hz.

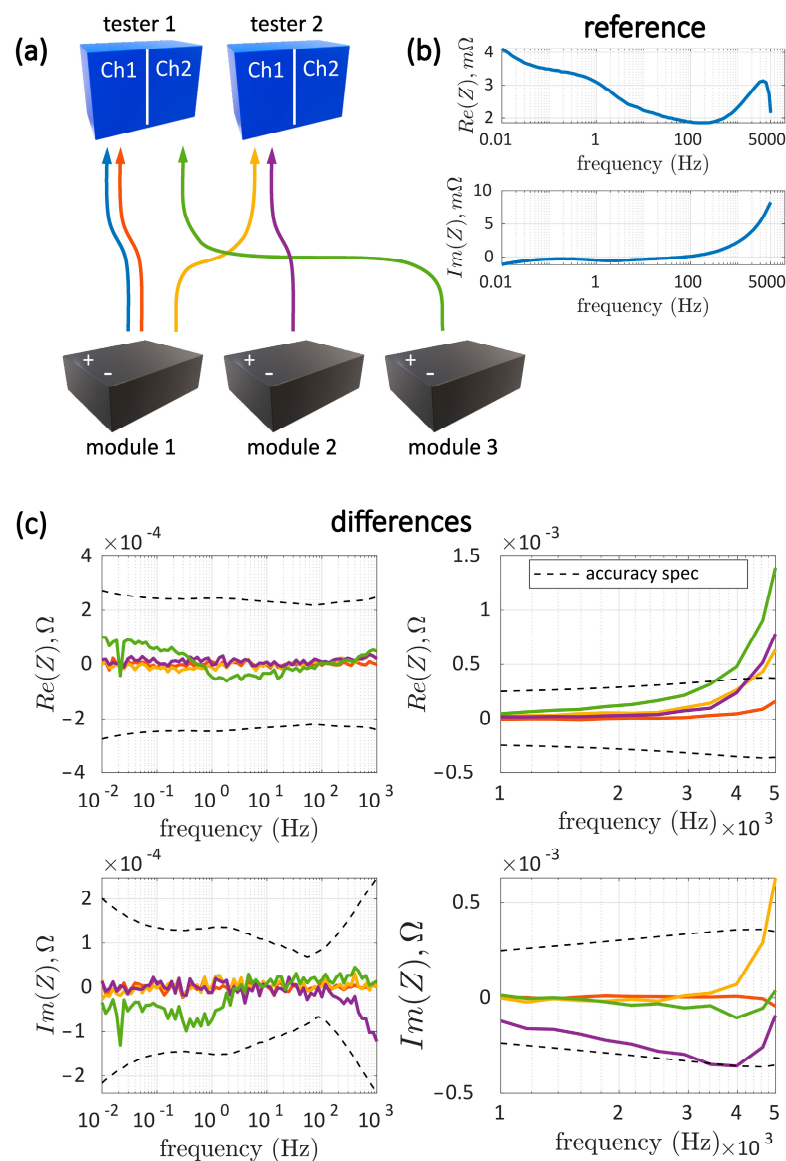


**Figure 6.** Comparison of EIS measurements performed with three channels of two testers and three battery modules at 50% SoC and 20 °C. (a) Sketch of the five different tester and module configurations. (b) Real and imaginary part of the reference measurement (module 1 at channel 1 of tester 1). (c) Differences in real and imaginary components of configurations #2–5 relative to configuration #1. The frequency axis is split between the left and right panels for better visualization. The dashed line indicates the accuracy specification of the tester. Trace colors match with the sketch (a).

The ohmic resistance, represented by the intersection of each curve with the  $x$ -axis, remains largely independent of the cycle number, with a mean value of  $1.83 \text{ m}\Omega \pm 10 \text{ }\mu\Omega$ . The local minimum point (represented with black circles) shows a significant correlation of the real impedance with the cycle number, increasing from  $2.3 \text{ m}\Omega$  @ cycle #300 to  $2.8 \text{ m}\Omega$  @ cycle #500, while the corresponding imaginary part shows only minimal variation of  $\sim 100 \text{ }\mu\Omega$ . Accordingly, the width of the semicircle, reflected by the distance of the intersection and the local minimum point, also shows a significant dependency on the cycle number. For the lowest frequency of  $10 \text{ mHz}$ , the real impedance increases from  $2.38 \text{ m}\Omega$  to  $3.55 \text{ m}\Omega$ , with a noticeable step change between fresh cells and cycle #300 (with the imaginary impedance showing a total increase of  $\sim 300 \text{ }\mu\Omega$ ). While the two impedance features of the local minimum point and the fixed frequency of  $10 \text{ mHz}$  provide a good sensitivity for the cycle number, the measurement efforts are relatively high because the determination of the

local minimum requires multiple points to be measured, and the measurement at 10 mHz is time-consuming. In contrast, the two features of the impedance at fixed frequencies left and right of the local minimum (3 Hz and 0.1 Hz) show a similar stable trend with the cycle number, having the advantage of faster measurements. In particular, the 0.1 Hz point shows a quasi-linear dependency of the real part of the impedance over the cycle number while the imaginary part stays approximately constant. The 3 Hz point shows the opposite behaviour, with a more sensitive imaginary part and less sensitive real part with respect to the cycle number.

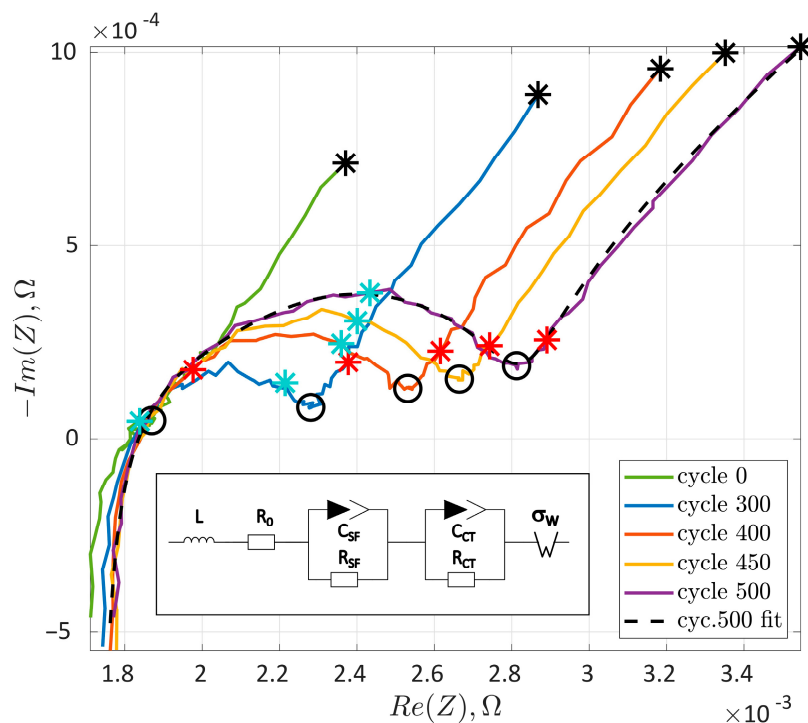


**Figure 7.** Evolution of distinct EIS features with the cycling number. Nyquist plot of EIS measurements for a single module at cycle numbers 300, 400, 450, and 500, at 50% SoC. Additionally, the fresh module with 0 cycles was also measured and is shown for comparison. Key impedance features are highlighted: the local minimum of the imaginary impedance (indicated by black circles) and the impedance at 0.01 Hz (marked with a black asterisk), 0.1 Hz (red asterisk), and 3 Hz (cyan asterisk). A fit of a modified Randles circuit to cycle #500 is shown as black dashed line (see main text).

The four experimentally determined impedance features are supported by a modified Randles circuit fit (Figure 7, dashed line for cycle #500), summarized as  $L + R_0 + [R_{SF} \parallel C_{SF}] + [R_{CT} \parallel C_{CT}] + \sigma_W$ . For the fit, two resonant elements in series are used, resulting in two semicircles that are significantly overlapping. From left to right, the extended Randles equivalent circuit includes a wiring inductance  $L$  describing, at high frequencies ( $>200$  Hz), the effect of wiring and electrode connections to the current collectors ( $L = 456$  nH). At roughly 100 Hz, the resistance of the electrolyte ( $R_0$ ) is related to the point where the imaginary part of the impedance reaches zero ( $R_0 = 1.67$  mOhm). A first semicircle describing the surface film resistance ( $R_{SF}$ ) and surface film capacitance ( $C_{SF}$ ) is obtained from the fit, corresponding to the electrolyte interphase and Lithium migration through the surface films. A second semicircle at a lower frequency describes the charge transfer resistance between the electrolyte and the solid surface ( $R_{CT}$ ), as well as the double-layer capacitance ( $C_{CT}$ ). Both semicircles are significantly overlapping between 1 Hz and 100 Hz. The Warburg impedance  $\sigma_W$  is then in series to the two semicircle elements, giving the

linear low-frequency region of the spectra (<1 Hz), which is characteristic of the materials diffusion processes at a solid-state electrode ( $\sigma_W = 1 \text{ mOhm/sqrt(s)}$ ).

Figure 8 shows an overview of the 0.1 Hz and 3 Hz features with respect to the cycle number and the SoC. The measurement uncertainty [16], derived from the previous chapter, is indicated by error bars for an SoC of 50%. Figure 8a shows the imaginary part for two modules at 3 Hz at four different SoCs, resulting in a smooth dependence on the cycle number and only a minor variation with SoC and the two modules. Figure 8b shows the same plot for the real part at 0.1 Hz, indicating a similar trend. Figure 8c shows a derived feature  $\Lambda = \frac{-Im(Z(3Hz))}{Re(Z(0.1Hz))}$ , which is based on the two features at 3 Hz and 0.1 Hz. Calculating the quotient has the advantage that all magnitude measurement errors are cancelled out and only phase error remains, resulting in significantly reduced uncertainty and error bars. Based on this analysis, the measurement uncertainty can be mapped to the cycle prediction uncertainty. The cycle prediction error span is around 25–42 cycles, taking into account an SoC range of 45–55%. The error analysis at the frequencies of 0.1 Hz and 3 Hz is performed under the conservative assumption of phase error that is one-tenth ( $\pm 0.2^\circ$ ) of the phase error at high frequencies ( $\pm 2^\circ$  above 100 Hz). This can be safely assumed since phase errors tend to linearly follow the frequency in minimum-phase systems (which the module tester does in the specific low-frequency range). In Figure 8d we show that the derived quotient feature  $\Lambda$  tracks the measured capacity of the modules, at a C-rate of C/20, showing distinct clusters for the various cycle numbers, suggesting it as a relevant feature for SoH determination.

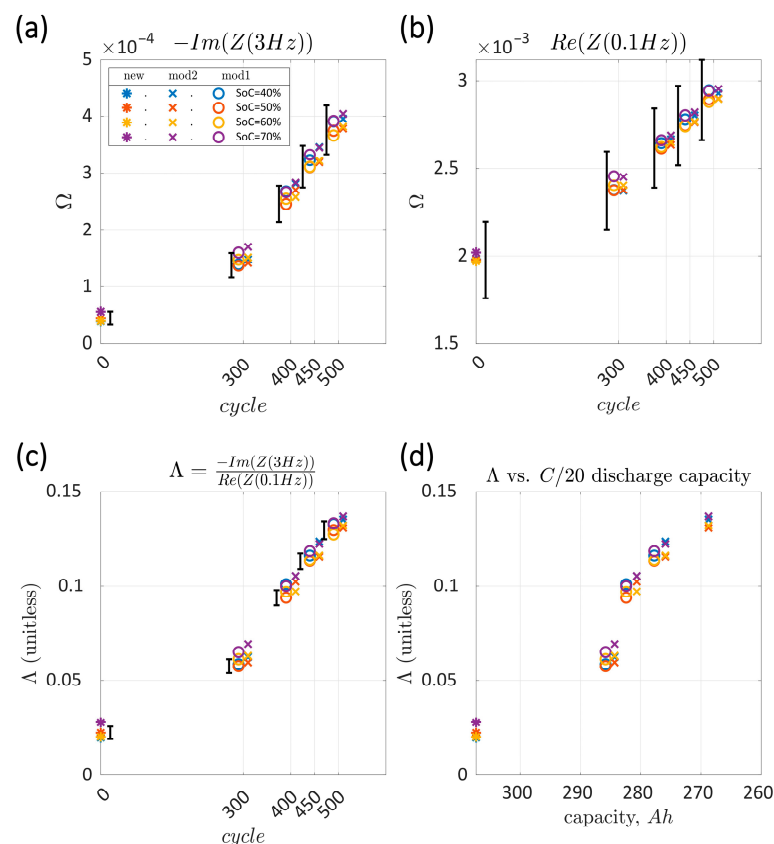


**Figure 8.** Evolution of distinct EIS features over cycle number. (a) Evolution of the first feature at 3 Hz for module 1 (circles) and module 2 (crosses) from cycle #300 to #500, with the new module (asterisk) shown at cycle #0. Data points are plotted across four SoC values ranging from 40% to 70%. Error bars represent the measurement uncertainty at a SoC of 50% (shown for module 1 and new module). (b) Evolution of the second feature derived at 0.1 Hz. (c) The derived feature  $\Lambda$  with significantly reduced uncertainty. (d) Feature  $\Lambda$  plotted against the measured C/20 discharge capacity.

#### 4. Conclusions

A calibration method for low-impedance EIS measurements is implemented and applied towards 10 kWh electric vehicle battery modules. Three different fixture configurations are tested and analyzed for their impact on EIS measurement accuracy. In addition, measurement errors are systematically assessed across five different tester module configurations, including temperature and SoC variations. The evolution of specific EIS features is examined as a function of cycle number, with up to 500 cycles.

Regarding the external factors that influence the accuracy of the impedance measurement, the results indicate that the module fixture wiring significantly impacts EIS measurement accuracy, particularly at mid-to-high frequencies. For example, incorrect sense-wire placements can introduce errors of up to 100% at 1 kHz in the imaginary part, while improper sense-point connections lead to errors of 2–5% at low frequencies. Both, the real and the imaginary components are typically affected, with an emphasis on the imaginary component at high frequencies. Similarly, temperature variations affect EIS measurements at low and medium frequencies, with a 6% increase in real impedance observed when the temperature drops from 23 °C to 20 °C. Finally, SoC module changes mostly influence low-frequency impedance behaviour. For example, when the SoC decreases from 50% to 30%, both the real and imaginary components show substantial changes at frequencies below 1 Hz. In summary, wiring configurations and mutual inductance influence the high-frequency impedance and they become the dominating error above ~100 Hz. In addition, at high frequencies, where electromagnetic rather than electrochemical mechanisms are the most significant error source, the error analysis is typically independent of the specific battery chemistry.

The repeatability of EIS measurements is tested across five different tester module configurations, including two testers and three modules. The EIS results remain highly consistent within the relevant frequency range of 50 mHz to 1 kHz, with variations limited to  $\pm 100 \mu\Omega$  for both real and imaginary impedance across three different modules. Comparing the same module across two different testers, deviations are even lower, staying within  $\pm 30 \mu\Omega$  up to 1 kHz.

The EIS evolution is studied with respect to the cycle numbers, and several key EIS features are analyzed based on a model-free and phenomenological approach. The ohmic resistance, representing the intersection of the EIS curve with the  $x$ -axis, remains largely independent of the cycle number, with a mean value of  $1.83 \text{ m}\Omega \pm 10 \mu\Omega$ . A strong correlation with the cycle number is obtained for the width of the semicircle at medium SoC levels, with the real part of the impedance increasing from  $2.3 \text{ m}\Omega$  at cycle #300 to  $2.8 \text{ m}\Omega$  at cycle #500. At the lowest frequency of 10 mHz, the real impedance also increases significantly, from  $2.38 \text{ m}\Omega$  to  $3.55 \text{ m}\Omega$ . While those two measures provide effective indicators of cycle-dependent impedance variations, there are practical limitations that include the extended measurement time and requirement for a large number of data points. A more efficient approach is introduced by deriving a quotient feature, also enhancing robustness by cancelling amplitude related measurement errors. This quotient feature demonstrates a strong correlation with the module capacity and distinct clustering across the cycle numbers, suggesting its potential as a reliable and efficient SoH indicator. Furthermore, only two points at relatively low frequencies (0.1 Hz and 3 Hz) need to be measured to determine this feature. This particular frequency range allows for cost-effective implementation of the measurement hardware while maintaining phase accuracy and avoiding drift problems, since the measurement is reasonably fast (well below one minute).

In summary, this study demonstrates the potential of EIS as a powerful tool for battery module characterization, provided that its requirements and limitations are carefully addressed through well-defined experimental setups. Reliable and repeatable EIS measure-

ments are achieved by optimizing fixture configurations, maintaining stable temperature conditions, ensuring precise SoC control, and applying proper test calibration procedures. These factors are particularly critical for obtaining accurate electrochemical insights, especially in the low- to mid-frequency domain, where impedance variations are most sensitive to battery state and ageing effects. Ensuring such measurement accuracy and traceability is essential for compliance with regulatory frameworks such as the UN Global Technical Regulation (GTR) No. 22 (in-vehicle battery durability for EVs) and for supporting the EU Battery Passport initiative, which mandates standardized performance metrics for transparency and lifecycle assessment.

**Author Contributions:** Conceptualization, A.L., F.K. and M.K.; methodology, A.P. and M.K.; software, A.P.; validation, F.K.; formal analysis, A.L. and M.K.; investigation, A.L.; resources, A.L. and F.K.; data curation, N.A.-Z.R.-S. and A.P.; writing—original draft preparation, N.A.-Z.R.-S., F.K. and M.K.; writing—review and editing, F.K. and M.K.; visualization, N.A.-Z.R.-S. and M.K.; supervision, F.K.; project administration, F.K.; funding acquisition, F.K. All authors have read and agreed to the published version of the manuscript.

**Funding:** The authors acknowledge funding from the European Union’s Horizon Europe research and innovation program under Grant Agreement No. 101135486 (DigiCell) and No. 101147457 (INERRANT).

**Data Availability Statement:** The data is partly available upon request.

**Acknowledgments:** The authors thank Manuel Moertelmaier from Keysight Technologies for the helpful technical discussions.

**Conflicts of Interest:** Authors Manuel Kasper, Nawfal Al-Zubaidi R-Smith and Ferry Kienberger were employed by the company Keysight Technologies Austria GmbH. Authors Arnd Leike and Aikaterini Papachristou were employed by the company BMW AG München. The authors declare that the research was conducted in the absence of any commercial or financial relationships that could be construed as a potential conflict of interest.

## References

- Offer, G.J.; Yufit, V.; Howey, D.A.; Wu, B.; Brandon, N.P. Module design and fault diagnosis in electric vehicle batteries. *J. Power Sources* **2012**, *206*, 383–392. [[CrossRef](#)]
- Belingardi, G.; Scattina, A. Battery Pack and Underbody: Integration in the Structure Design for Battery Electric Vehicles—Challenges and Solutions. *Vehicles* **2023**, *5*, 498–514. [[CrossRef](#)]
- Shu, X.; Yang, W.; Yang, B.; Wei, K.; Punyawudho, K.; Liu, C. Research on EIS characterization and internal morphological changes of LIBs during degradation process. *Eng. Fail. Anal.* **2024**, *155*, 107764. [[CrossRef](#)]
- Kehl, D.; Jennert, T.; Lienesch, F.; Kurrat, M. Electrical Characterization of Li-Ion Battery Modules for Second-Life Applications. *Batteries* **2021**, *7*, 32. [[CrossRef](#)]
- Wang, Y.; Xiang, H.; Soo, Y.-Y.; Fan, X. Aging mechanisms, prognostics and management for lithium-ion batteries: Recent advances. *Renew. Sustain. Energy Rev.* **2025**, *207*, 114915. [[CrossRef](#)]
- Li, Y.; Guo, J.; Pedersen, K.; Gurevich, L.; Stroe, D.-I. Recent Health Diagnosis Methods for Lithium-Ion Batteries. *Batteries* **2022**, *8*, 72. [[CrossRef](#)]
- Kasper, M.; Leike, A.; Thielmann, J.; Winkler, C.; Al-Zubaidi R-Smith, N.; Kienberger, F. Electrochemical impedance spectroscopy error analysis and round robin on dummy cells and lithium-ion-batteries. *J. Power Sources* **2022**, *536*, 231407. [[CrossRef](#)]
- Hu, W.; Peng, Y.; Wei, Y.; Yang, Y. Application of Electrochemical Impedance Spectroscopy to Degradation and Aging Research of Lithium-Ion Batteries. *J. Phys. Chem. C* **2023**, *127*, 4465–4495. [[CrossRef](#)]
- Galeotti, M.; Cinà, L.; Giannanco, C.; Cordiner, S.; Di Carlo, A. Performance analysis and SOH (state of health) evaluation of lithium polymer batteries through electrochemical impedance spectroscopy. *Energy* **2015**, *89*, 678–686. [[CrossRef](#)]
- Mašlán, S.; He, H.; Bergsten, T.; Seitz, S.; Heins, T.P. Interlaboratory comparison of battery impedance analyzers calibration. *Measurement* **2023**, *218*, 113176. [[CrossRef](#)]
- UN GTR No.22 (In-Vehicle Battery Durability for Electrified Vehicles) | UNECE. Available online: <https://unece.org/transport/documents/2022/04/standards/un-gtr-no22-vehicle-battery-durability-electrified-vehicles> (accessed on 27 March 2025).
- Patrone, G.L.; Paffumi, E. Experimental Application of the Global Technical Regulation on In-Vehicle Battery Durability. *Batteries* **2023**, *9*, 454. [[CrossRef](#)]

13. Butera, A.; Gatteschi, V. EU Battery Regulation and the Role of Blockchain in Creating Digital Battery Passports. In Proceedings of the 2024 6th Conference on Blockchain Research & Applications for Innovative Networks and Services (BRAINS), Berlin, Germany, 9–11 October 2024; pp. 1–4.
14. Kasper, M.; Moertelmaier, M.; Ragulskis, M.; Al-Zubaidi R-Smith, N.; Angerer, J.; Aufreiter, M.; Romero, A.; Krummacher, J.; Xu, J.; Root, D.E.; et al. Calibrated Electrochemical Impedance Spectroscopy and Time-Domain Measurements of a 7 kWh Automotive Lithium-Ion Battery Module with 396 Cylindrical Cells. *Batter. Supercaps* **2023**, *6*, e202200415. [[CrossRef](#)]
15. Keysight Technologies SL1007A Specification. Available online: <https://www.keysight.com/us/en/assets/7018-06654/data-sheets/5992-4044.pdf> (accessed on 17 October 2025).
16. Moradpour, A.; Kasper, M.; Hoffmann, J.; Kienberger, F. Measurement Uncertainty in Battery Electrochemical Impedance Spectroscopy. *IEEE Trans. Instrum. Meas.* **2022**, *71*, 1006209. [[CrossRef](#)]

**Disclaimer/Publisher’s Note:** The statements, opinions and data contained in all publications are solely those of the individual author(s) and contributor(s) and not of MDPI and/or the editor(s). MDPI and/or the editor(s) disclaim responsibility for any injury to people or property resulting from any ideas, methods, instructions or products referred to in the content.